Magnetic anisotropy reveals the depositional and postdepositional history of a loess-paleosol sequence at Nussloch (Germany)

Samuel N. Taylor, France Lagroix

AGU PUBLICATIONS

JGR

Journal of Geophysical Research: Solid Earth

RESEARCH ARTICLE
10.1002/2014JB011803

Key Points:
- Nussloch P8 loess sequence archives both primary and secondary AMS fabrics
- Secondary AMS fabrics result from permafrost-related reworking
- Inferred paleowind directions are speculative with magnetite content <0.03 wt %

Correspondence to:
F. Lagroix,
lagroix@ipgp.fr

Citation:
Taylor, S. N., and F. Lagroix (2015), Magnetic anisotropy reveals the depositional and postdepositional history of a loess-paleosol sequence at Nussloch (Germany), *J. Geophys. Res. Solid Earth*, *120*, 2859–2876, doi:10.1002/2014JB011803.

Received 25 NOV 2014
Accepted 29 MAR 2015
Accepted article online 3 APR 2015
Published online 7 MAY 2015

Magnetic anisotropy reveals the depositional and postdepositional history of a loess-paleosol sequence at Nussloch (Germany)

Samuel N. Taylor[1] and France Lagroix[1]

[1]Institut de Physique du Globe de Paris, Sorbonne Paris Cité, Université Paris Diderot, CNRS, Paris, France

Abstract Anisotropy of magnetic susceptibility (AMS) is employed as a tool to unravel the depositional history of the 17 m thick Nussloch P8 Weichselian loess sequence located 10 km south of Heidelberg, Germany. Through an AMS study, the primary aeolian depositional origin of the magnetic fabrics is evaluated, and overprinting due to postdepositional reworking and/or deformation is identified. Primary fabrics along the P8 sequence are defined by near-vertical K_{MIN} axes and horizontal foliations. Eight intervals display secondary fabrics, characterized by either prolate orientation distributions or oblate orientation distributions with dipping foliation planes. These postdepositional fabrics are associated with laminated loess and tundra gley horizons. It is proposed that increased moisture (due to higher precipitation or enhanced snowmelt) and repeated cryogenic processes were able to reorganize and rework the accumulated loess. Primary aeolian fabrics are archived within 6.45 m of cumulated depth or 38% of the profile and dominantly within the Upper Pleniglacial units. Even though maximum susceptibility axes of primary fabrics are statistically well resolved at the specimen ($\varepsilon_{12} = 10.1° \pm 8.6$) and population ($\varepsilon_{12} = 6°$) level, any inferred paleowind directions from the magnetic lineation remains speculative given the low concentration of ferrimagnetic minerals (<0.03 wt %). Tundra gley horizons upprofile display primary magnetic fabrics and no major changes in the degree of anisotropy or AMS orientation distributions. This suggests a weakening in gley-induced diagenesis and therefore favorable environmental conditions needed (moisture and presence of permafrost active layer) to initiate their formation in loess deposits. Finally, pedogenesis has not played an important role in modifying the magnetic fabric since paleosols display the same magnetic fabrics observed in primary loess.

1. Introduction

Anisotropy of magnetic susceptibility (AMS) of rocks and sediments is used for petrofabric and structural studies [e.g., *Rochette et al.*, 1992; *Borradaile and Henry*, 1997] and arises from the cumulative magnetic anisotropy of all minerals within a specimen. AMS of ferromagnetic (in a broad sense) grains with high internal demagnetization fields, such as magnetite and maghemite, is dominated by shape anisotropy (preferred dimensional orientation) [e.g., *Tarling and Hrouda*, 1993; *Borradaile and Henry*, 1997]. Otherwise, a mineral's AMS is controlled by its crystal symmetry [e.g., *Rochette et al.*, 1992; *Borradaile and Jackson*, 2010]. Magnetic fabric analyses are universally applicable, rapid to measure, they simultaneously analyze the orientations of all grains within a sample; are nondestructive; and can be used to quantify numerous geological processes [e.g., *Kligfield et al.*, 1981; *Tarling and Hrouda*, 1993; *Borradaile and Henry*, 1997; *Borradaile and Jackson*, 2010]. In sediments, AMS can relate to depositional processes [e.g., *Tarling and Hrouda*, 1993; *Tauxe*, 2002]. A primary aeolian sedimentary fabric is characterized by a magnetic foliation that dominates over a magnetic lineation, which may or may not be present [e.g., *Lagroix and Banerjee*, 2002]. The minimum axis of the AMS ellipsoid (K_{MIN}) represents the pole of the magnetic foliation and for an aeolian deposition of silt-sized particles, will also be the pole of the depositional bedding plane. The maximum axis (K_{MAX}) of the AMS ellipsoid has been reported, in some studies, to define a magnetic lineation interpreted as an indicator of the wind-deposited dust transport direction (e.g., Siberia [*Matasova et al.*, 2001], Alaska [*Lagroix and Banerjee*, 2002, 2004b], Poland and Ukraine [*Nawrocki et al.*, 2006], and Hungary [*Bradák*, 2009]).

After deposition, the primary fabric recorded in loess is vulnerable to postdepositional reworking through redeposition, pedogenesis, bioturbation, slumping, and periglacial processes. One may expect textural contrasts to arise from the above processes (pedogenesis excluded), but given the homogeneity of loess granulometry and mineralogy, textural contrasts are seldom observed in the field. Therefore, differentiating

between primary depositional magnetic fabrics, retained by pristine loess, from secondary magnetic fabrics resulting from postdepositional processes is a main objective. In Alaska, *Lagroix and Banerjee* [2004a] provided evidence for postdepositional deformation within loess units associated with permafrost dynamics during rapid warm periods. The sensitivity of AMS to palaeoclimate has been further investigated in Chinese loess, where the declination of K_{MAX} (direction of magnetic lineation) was used as a proxy for rapid fluctuations in summer/winter monsoon seasons, while stronger summer monsoons are postulated to play a major role in dust particle orientation and consolidation [*Zhu et al*., 2004; *Zhang et al*., 2010].

The extensively analyzed Weichselian Pleniglacial loess sequences from Nussloch (49°18′59″N, 8°43′54″E), located 10 km south of Heidelberg, Germany, in an active quarry, have become key records for palaeoenvironmental and palaeoclimate change in western Europe [see *Antoine et al*., 2001, 2009; *Rousseau et al*., 2002, 2007; *Lang et al*., 2003; *Hatté and Guiot*, 2005; *Moine et al*., 2005, 2008; *Bibus et al*., 2007; *Kadereit et al*., 2013; *Gocke et al*., 2014; *Taylor and Lagroix*, 2014]. Studies have shown that these loess-paleosol deposits have the ability to record millennial scale climate variations, based upon a comparison of sediment grain size and dust records from Greenland ice cores [*Rousseau et al*., 2007; *Antoine et al*., 2009]. Recent research has identified tundra gley horizons and paleosols as markers for periods of climate amelioration that are linked to Dansgaard-Oeschger warming events [*Rousseau et al*., 2007; *Antoine et al*., 2009]. These horizons are associated with redoxomorphic processes induced by waterlogging: a result of active layer deepening and increased surface moisture permitting water to percolate and saturate above an impermeable (permafrost) boundary. *Taylor and Lagroix* [2014] recently characterized tundra gleys as having a secondary control on the magnetic mineral assemblage through postdepositional dissolution of fine-grained magnetite associated with waterlogging in discrete thin (on average 10 cm) depth intervals and sometimes located outside of the field identified tundra gley unit boundaries. It may be expected for postdepositional reworking of loess in water-saturated conditions to lead to changes in mineral fabric detectable with AMS. Such a study has never been undertaken at Nussloch. The previous environmental magnetism study by *Taylor and Lagroix* [2014] on the P4 sequence at Nussloch was only sampled for bulk nonoriented material throughout the Upper Pleniglacial units. A new profile was therefore necessary to conduct an AMS study and evaluate the pristine or reworked nature of the deposits.

There are still outstanding questions with regards to western European loess, such as the sources of material and the distance and direction of dust transport to compare with climate models. Based upon the orientation of loess gredas [*Leger*, 1990; *Antoine et al*., 2001], sediment grain-size sorting (from north to south Europe) [e.g., *Huijzer and Vandenberghe*, 1998], recent climate modeling [*Sima et al*., 2009], and geochemical data [*Rousseau et al*., 2014], deflation areas are postulated to arise in the English Channel-North Sea Basin during glacial periods, with intense storms producing winds from the NW-NNW direction. In addition, sediment grain-size analyses suggest that an increase in local deflation of coarse-grained sediment from river plains could be incorporated into the western European deposits [e.g., *Antoine et al*., 2009; *Rousseau et al*., 2014]. An AMS study can answer several questions to enable a better understanding of the depositional and postdepositional history of the Nussloch deposits: How is the aeolian-deposited mineral fabric affected by the development of tundra gley soils or by the redoxomorphic features associated with them? Have any primary magnetic fabrics been preserved in loess intervals? Can prevailing dust transport directions be recovered in primary loess? Consequently, this will give a better interpretation of magnetic and nonmagnetic climate proxies retrieved and chronological data obtained from Nussloch. To our knowledge, this is the first magnetic anisotropy study of Nussloch loess sequences.

2. Sampling and Methodology

The Nussloch P8 loess sequence was exposed, described, and sampled in October 2012. Covering the last glacial cycle (specifically the Upper and Middle Pleniglacial, UPL and MPL), this 17 m section contains loess layers (both homogeneous and laminated), tundra gley horizons, and buried boreal brown soils/cambisols (hereafter referred to as palaeosols) as the main stratigraphical components (Figure 1). The 0 m point marks the Holocene topsoil, where depths increase downprofile with the 17 m mark at the top of the Eemian palaeosol surface (Figure 1). The Eltviller Tuff (ET), a regional stratigraphic marker [*Juvigné and Semmel*, 1981; *Pouclet and Juvigné*, 2009], is located at 3.75–3.70 m. This is the first publication of Nussloch P8 sequence, but the stratigraphic unit numbers (increasing upprofile) follow the nomenclature of previously published

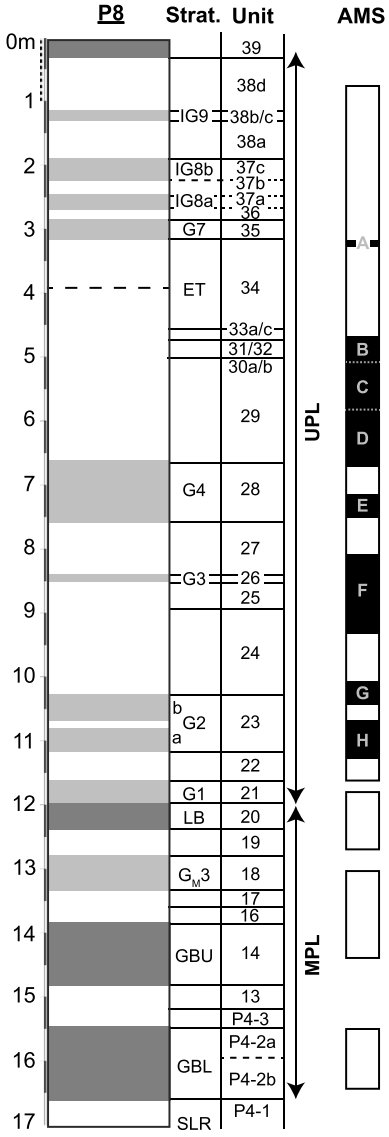

Figure 1. Stratigraphy of the P8 Nussloch section, sampled continuously for bulk material ($N_{bulk} = 340$) and discretely for oriented specimens ($n_{oriented} = 863$) at 5 cm intervals. The dashed line locates the Eltviller tuff (ET). The light grey bands on the stratigraphy mark the tundra gley horizons, while the dark grey bands mark the paleosols. G = major tundra gley, IG = incipient tundra gley, LB = Lohner Boden, GBU = Gräselberger Boden (upper), GBL = Gräselberger Boden (lower), UPL = Upper Pleniglacial, and MPL = Middle Pleniglacial. The unit numbers follow the nomenclature established for previous Nussloch profiles [see *Antoine et al.*, 2001, 2002, 2009]. The right column displays the AMS-sampled depths and highlights intervals that have undergone postdepositional reworking (black bars). See section 3.2 for further explanations.

sequences sampled in the same quarry. A detailed sedimentary and pedological description of the stratigraphic units can be found in *Antoine et al.* [2001, 2009]. The most recent compilation of published age determinations for Nussloch is reported in *Kadereit et al.* [2013]. They argue for an age to the Lohner Boden (LB) paleosol younger than 35 ka but older than 30 ka. This would alter the previously inferred correlations of tundra gley and paleosol horizons to Greenland interstadial episodes proposed in *Rousseau et al.* [2007] and *Antoine et al.* [2009].

Bulk sampling was conducted following the continuous column protocol described in *Antoine et al.* [2009] at a 5 cm depth resolution (beginning from 0.3 m depth), resulting in 338 bulk samples. Geographically oriented specimens were sampled discretely in the field at a depth interval of 5 cm. At each of the 282 sampling depths, 3 to 4 specimens were extracted rendering a suite of 863 specimens. The cubic specimens (approximately 8 cm^3) were acquired with a piston-plunge hand sampling method, using little or no hammering to insert a sampler into a cleaned, vertical loess surface. A vibration-free hammer was used when necessary. *Lagroix and Banerjee* [2004a] showed that their results were not influenced by any sampling-induced deformations by using this method. The azimuth, dip, and tilt (*y* axis deviation from horizontal) of the square-sectioned piston were measured using a Brunton clinometer. A similar technique to this has also been previously identified as the best method for obtaining reliable AMS results from soft loess deposits [*Jordanova et al.*, 1996]. Carbonate concretions and large root traces were avoided during sampling. Krotovinas were not observed along the profile. Depths between 15.45–14.50 m and 0.70–0.0 m were unsampled because the sediment was poorly consolidated due to higher sand content and greater root traces, respectively. No samples were collected through 13.1–12.7 m and 11.80–11.65 m depth intervals.

The AMS of the oriented specimens was measured on a Kappabridge KLY-3 susceptibility bridge in 300 Am^{-1} and 875 Hz alternating field, following the spinning specimen method about three perpendicular planes. Resulting AMS ellipsoids were computed using PaleoMac [*Cogné*, 2003], which uses the statistical formulas of *Jelinek* [1981] following *Hext* [1963]. The principal susceptibility axes that define an ellipsoid with three orthogonal axes for each specimen are labelled: K_{MAX}, K_{INT}, and K_{MIN}. Each of the principle axes has been normalized by the mean susceptibility K_{mean} calculated from the AMS principal axes. For a single specimen, the orientation and magnitude of each axes correspond to the nonscaled principal eigenparameters, where $K_{MAX} \geq K_{INT} \geq K_{MIN}$, and together, they define the shape and eccentricity of the AMS ellipsoid. An oblate shape has $K_{MIN} < 1$ and both K_{MAX} and $K_{INT} > 1$. A

prolate shape has both K_{MIN} and $K_{INT} < 1$ and $K_{MAX} > 1$. A neutral (isotropic) shape occurs when all axes have a value of 1. A 95% confidence ellipse with semiaxes (ε) oriented parallel to the principal axis planes describes the uncertainty around principal axes orientations [see *Tauxe*, 2002; *Lagroix and Banerjee*, 2004b]. The half-angle uncertainty of K_{MAX} in the plane joining K_{INT} and in the plane joining K_{MIN} is defined by the semiaxes ε_{12} and ε_{13}, respectively. K_{MAX}, K_{INT}, and K_{MIN} are denoted as 1, 2, and 3, respectively, in the subscript notation of ε. The corrected degree of anisotropy (*Pj*) and the shape of the AMS ellipsoid (*Tj*), as defined by *Jelinek* [1981], are defined as follows:

$$Pj = \exp\left(\sqrt{2\left[\left(\ln\left(\frac{k_{MAX}}{k}\right)\right)^2 + \left(\ln\left(\frac{k_{INT}}{k}\right)\right)^2 + \left(\ln\left(\frac{k_{MIN}}{k}\right)\right)^2\right]}\right) \quad (1)$$

$$Tj = \frac{(2\ln k_{INT} - \ln k_{MAX} - \ln k_{MIN})}{(\ln k_{MAX} - \ln k_{MIN})} \quad (2)$$

The shape of the AMS ellipsoid is described a prolate or rod shape when *Tj* equals −1 to 0 and an oblate or disk shape when *Tj* equals 0 to +1. It is also be interesting to evaluate the contribution of the magnetic foliation (*F*) and the magnetic lineation (*L*) to the degree of anisotropy (*P*) following the definition of *Nagata* [1961], where *P* is the K_{MAX}/K_{MIN} ratio, *L* is the K_{MAX}/K_{INT} ratio, and *F* is the K_{INT}/K_{MIN} ratio.

Complementary rock magnetic analyses were conducted on the collected bulk samples. Low field magnetic susceptibility (χ_{bulk}) was measured at room temperature using a Kappabridge KLY-3. Hysteresis loops and backfield isothermal remanent magnetization (IRM) analyses were measured using a Princeton Measurements Vibrating Sample Magnetometer. Hysteresis loops were acquired in a maximum field of ±1.5 T. The ferrimagnetic susceptibility (χ_{ferri}) was calculated by subtracting the high field slope (χ_{hifi}) of the uncorrected hysteresis loops from χ_{bulk}. The high field slope was calculated over the 1.05 to 1.5 T range (equal to 70% of the maximum field). An IRM imparted in a +1 T magnetic field was subjected to increasingly higher backfields (denoted by minus sign) at −100 mT steps up to −1 T. IRM measured following the −100 mT step ($IRM_{-100\,mT}$), the −300 mT step ($IRM_{-300\,mT}$), and the −1 T step ($IRM_{-1\,T}$) were used to calculate the *S* ratio and hard isothermal remanent magnetization (HIRM) parameters. "Hard" isothermal remanent magnetization (HIRM) was calculated from backfield curves by

$$HIRM = IRM_{-300\,mT} - IRM_{-1T} \quad (3)$$

Anhysteretic remanent magnetization (ARM) was acquired using an LDA-3 AF-Demagnetizer in a decaying alternating field from a peak of 100 mT to 0 mT superimposed by a constant direct current (DC) field of 0.05 mT. The acquired ARM was measured using a 2G DC superconducting quantum interference device cryogenic magnetometer.

3. Results

For the purposes of this study, an age model for P8 was constructed using a compilation of available age determinations published from other Nussloch profiles (Table 1 and Figure 2) but principally from P4. There are no chronological data yet available for P8. First, the depth scale of the P4 profile was correlated to the reference P8 depth scale using the AnalySeries 2.0 software [*Paillard et al.*, 1996]. The correlation was performed using only three tie points and resulted in a correlation coefficient of 0.75 (Figure 2a). The three tie points were (1) P4 (0.0 m)–P8 (0.7 m), justified by the fact that the 0 m mark at P4 was 1 m below the surface and P8 is 0.3 m below the surface; (2) P4 (4.20 m)–P8 (3.75 m) correlating the Eltviller Tuff (ET) tephra occurrence in both profiles; and (3) P4 (9.72 m)–P8 (9.10 m) providing a lower boundary tie point needed because P4 is not as stratigraphically extended as P8. Second, the published ages (see Table 1) were transposed onto the P8 depth scale via stratigraphic unit correlations when data originate from profiles other than P4 [*Gocke et al.*, 2014] and via the correlated depth scales for data that originate from P4 or previously correlated to P4 by others [*Rousseau et al.*, 2007; *Tissoux et al.*, 2010]. Ages from *Bibus et al.* [2007] were assigned following a mixture of stratigraphic unit correlations and correlated depth scaling. Third, a simplistic age model was defined from Figure 2b by linear best fitting data across the UPL units and the MPL units. Sedimentation rates are high in the major loess unit of the UPL (0.53 mm yr^{-1}) and low (0.17 mm yr^{-1}) through the MPL when paleosols developed. Overall, this constructed age model results in

Table 1. List of Published Age Determinations for Other Nussloch Profile Used Here to Construct the Age Model for the P8 Profile

Depth P8 (m)	Age (kyr)	Method	Profile	Profile + Reference
1.00	17.6 ± 1.7	optically stimulated luminescence (OSL) (quartz)	P_{2011}	*Gocke et al.* [2014]
2.70	19.3 ± 3.0	infrared stimulated luminescence (IRSL)	P4	*Rousseau et al.* [2007]
3.90	27.5 ± 1.8	OSL (quartz)	P_{2011}	*Gocke et al.* [2014]
4.40	23.1 ± 1.8	OSL (quartz)	P4	*Tissoux et al.* [2010]
4.75	23.5 ± 2.3	OSL (quartz)	P_{2011}	*Gocke et al.* [2014]
5.25	23.2 ± 2.6	IRSL	P4	*Bibus et al.* [2007]
5.70	18.6 ± 2.0	IRSL	P4	*Bibus et al.* [2007]
5.90	20.7 ± 2.2	IRSL	P4	*Bibus et al.* [2007]
6.25	21.0 ± 2.3	IRSL	P4	*Bibus et al.* [2007]
6.50	29.4 ± 1.7	OSL (quartz)	P_{2011}	*Gocke et al.* [2014]
6.85	23.9 ± 0.2	^{14}C	P4	*Bibus et al.* [2007]
7.30	19.1 ± 2.4	IRSL	P4	*Bibus et al.* [2007]
7.70	24.4 ± 2.9	IRSL	P4	*Bibus et al.* [2007]
7.96	31.1 ± 2.9	OSL (quartz)	P_{2011}	*Gocke et al.* [2014]
7.98	19.4 ± 2.2	IRSL	P4	*Bibus et al.* [2007]
8.35	19.7 ± 2.3	IRSL	P4	*Bibus et al.* [2007]
8.48	24.8 ± 0.2	^{14}C	P4	*Bibus et al.* [2007]
8.58	23.4 ± 2.7	IRSL	P4	*Bibus et al.* [2007]
8.98	25.2 ± 2.7	IRSL	P4	*Bibus et al.* [2007]
9.00	34.9 ± 2.2	OSL (quartz)	P_{2011}	*Gocke et al.* [2014]
9.38	27.7 ± 3.0	IRSL	P4	*Bibus et al.* [2007]
9.76	29.5 ± 2.0	OSL (quartz)	P4	*Tissoux et al.* [2010]
9.95	25.1 ± 2.8	IRSL	P4	*Bibus et al.* [2007]
10.00	29.3 ± 7.4	IRSL	P4	*Rousseau et al.* [2007]
10.34	32.0 ± 3.7	IRSL	P4	*Bibus et al.* [2007]
10.65	30.9 ± 3.6	IRSL	P4	*Rousseau et al.* [2007]
10.78	25.9 ± 3.7	IRSL	P4	*Bibus et al.* [2007]
11.24	26.0 ± 2.9	IRSL	P4	*Bibus et al.* [2007]
11.26	28.2 ± 4.1	IRSL	P4	*Rousseau et al.* [2007]
11.65	31.7 ± 0.3	^{14}C	P4	*Bibus et al.* [2007]
12.10	26.7 ± 3.4	IRSL	P4	*Bibus et al.* [2007]
12.20	35.1 ± 2.3	OSL (quartz)	P_{2011}	*Gocke et al.* [2014]
12.60	40.8 ± 6.2	IRSL	P4	*Rousseau et al.* [2007]
14.40	34.0 ± 3.7	IRSL	P4	*Bibus et al.* [2007]
15.40	36.6 ± 3.9	IRSL	P4	*Bibus et al.* [2007]
16.50	57.2 ± 5.7	IRSL	P4	*Bibus et al.* [2007]
17.00	54.2 ± 4.2	OSL (quartz)	P4	*Tissoux et al.* [2010]

slightly younger ages when compared with previously published models by *Rousseau et al.* [2007] and *Antoine et al.* [2009]. Our model considers a larger data set of ages than either of the mentioned studies, which may explain the discrepancy.

3.1. Bulk Magnetic Properties

The previous rock magnetic study at Nussloch (UPL P4 sequence [*Taylor and Lagroix*, 2014]) identified magnetite and goethite as the major components of the mineral magnetic assemblage. The presence of hematite was not excluded, but neither room temperature nor low-temperature magnetism data provided convincing evidence for its occurrence. Bulk ferrimagnetic concentration parameters (χ, χ_{ferri}, M_S, $IRM_{-300\,mT}$, and $IRM_{1\,T}$) were shown to be dominantly controlled by variations in multidomain (MD) magnetite particles of detrital origin since no correlation was observed with ARM or χ_{ARM}. The latter being more sensitive to single domain (SD) and pseudo-single domain (PSD) particles. Dissolution of single to pseudo-single domain (SD-PSD) magnetite in certain depth intervals was imprinted on the magnetic record and identified by decreases in χ, M_S, and ARM and increases in $ARM/IRM_{-300\,mT}$ with respect to the surrounding material. Dissolution was a consequence of redoxomorphic processes induced by waterlogging. Lastly, *Taylor and Lagroix* [2014] demonstrated that for the magnetic mineral assemblage of the Nussloch deposits, $ARM/IRM_{-300\,mT}$ more accurately tracks changes in mean ferrimagnetic grain size than the more commonly used χ_{ARM}/χ_{ferri} ratio due to the absence of superparamagnetic (SP) particles. They

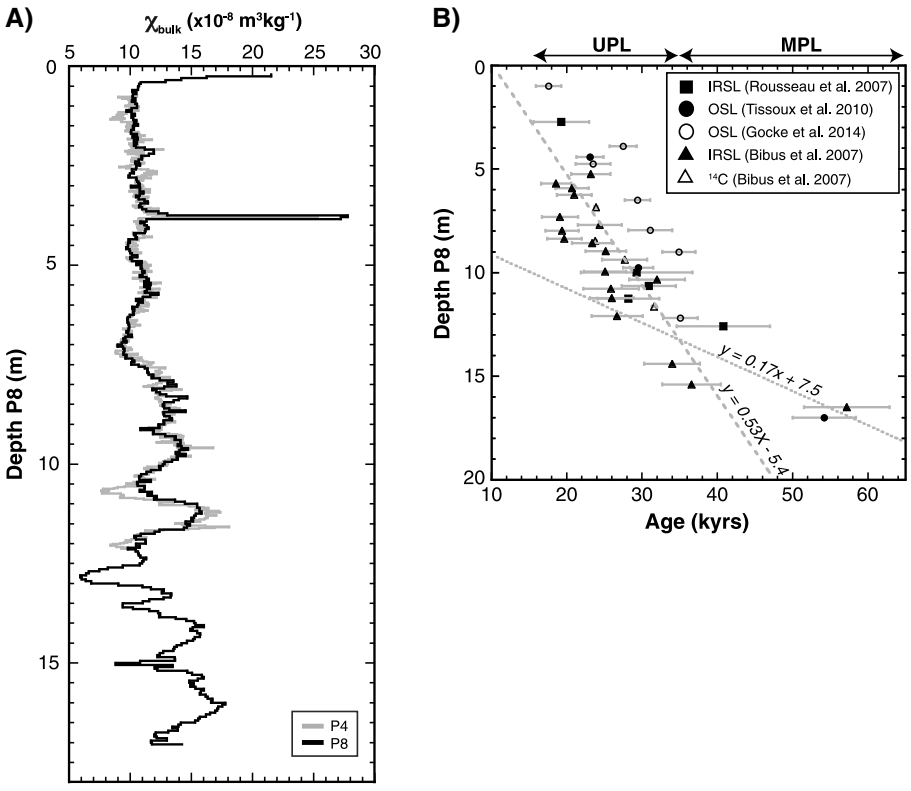

Figure 2. (a) Depth trends in bulk magnetic susceptibility (χ_{bulk}) for the Nussloch P4 [*Taylor and Lagroix*, 2014] and P8 (this study) profiles. The P4 χ_{bulk} series has been rescaled to the P8 depths after correlation. (b) Age model for the P8 sequence based upon a compilation of published OSL, IRSL, and ^{14}C age determinations from other sequences within the Nussloch quarry. UPL: Upper Pleniglacial and MPL: Middle Pleniglacial. See section 3 for further information on the correlation and age model construction.

demonstrated absence of SP particles from the lack of frequency dependence of the magnetic susceptibility measured at room temperature in a 160 A/m alternating field at three to five frequencies ranging from 10 to 1000 Hz. Therefore, a ferrimagnetic grain-size ratio based uniquely on two remanence parameters, which excludes SP grain sizes, is not penalizing. Moreover, the important high-coercivity component, attested by *S* ratio data (Figure 2), renders χ_{ferri} less accurate than IRM$_{-300\ mT}$ as a ferrimagnetic concentration parameter due to the method by which χ_{ferri} is calculated.

Variations in P8 bulk magnetic parameters and ratios between 12.0 and 0.3 m (~33–12 ka) (Figure 2) follow the same trend as those along Nussloch P4 [*Taylor and Lagroix*, 2014] distanced by ~100 m. An absence of SP grains at room temperature is observed throughout all samples within the P8 sequence. The reproducibility of results along different profiles within the quarry attests to the regional significance of the observed variations and allows a similar interpretation of rock magnetic parameters along P8 to those argued for P4 and restated above. Following the criteria exposed in *Taylor and Lagroix* [2014], six intervals have undergone dissolution of fine-grained ferrimagnetic minerals along P8, and similar to P4, these are associated with tundra gley horizons (G2: 11.15–10.90 m; G3: 8.45–8.40 m; G4: 7.55–7.35 m, 7.1–7.0 m, and 6.75–6.65 m; and G7: 3.05–2.95 m (Figure 8)).

However, the modern soil and palaeosols (Lohner Soil (LB), Upper Gräselberger Soil (GBU), and Lower Gräselberger Soil (GBL)) were not sampled at P4 and are characterized here in P8. The topsoil is characterized by a peak in ferrimagnetic concentration parameters (χ_{bulk}, χ_{ferri}, M_S, IRM$_{1\ T}$ (not shown), and ARM) and ARM/IRM$_{-300\ mT}$ (Figure 3). The palaeosols found between 17 and 12 m (~56–33 ka) equally display a marked increase χ_{bulk}, ARM, and ARM/IRM$_{-300\ mT}$ (Figure 3), inferring that there is an increase in the concentration and decrease in grain size of ferrimagnetic particles. This can be attributed to the in situ development of fine-grained magnetite/maghemite particles (but not SP), attesting to the pedogenic

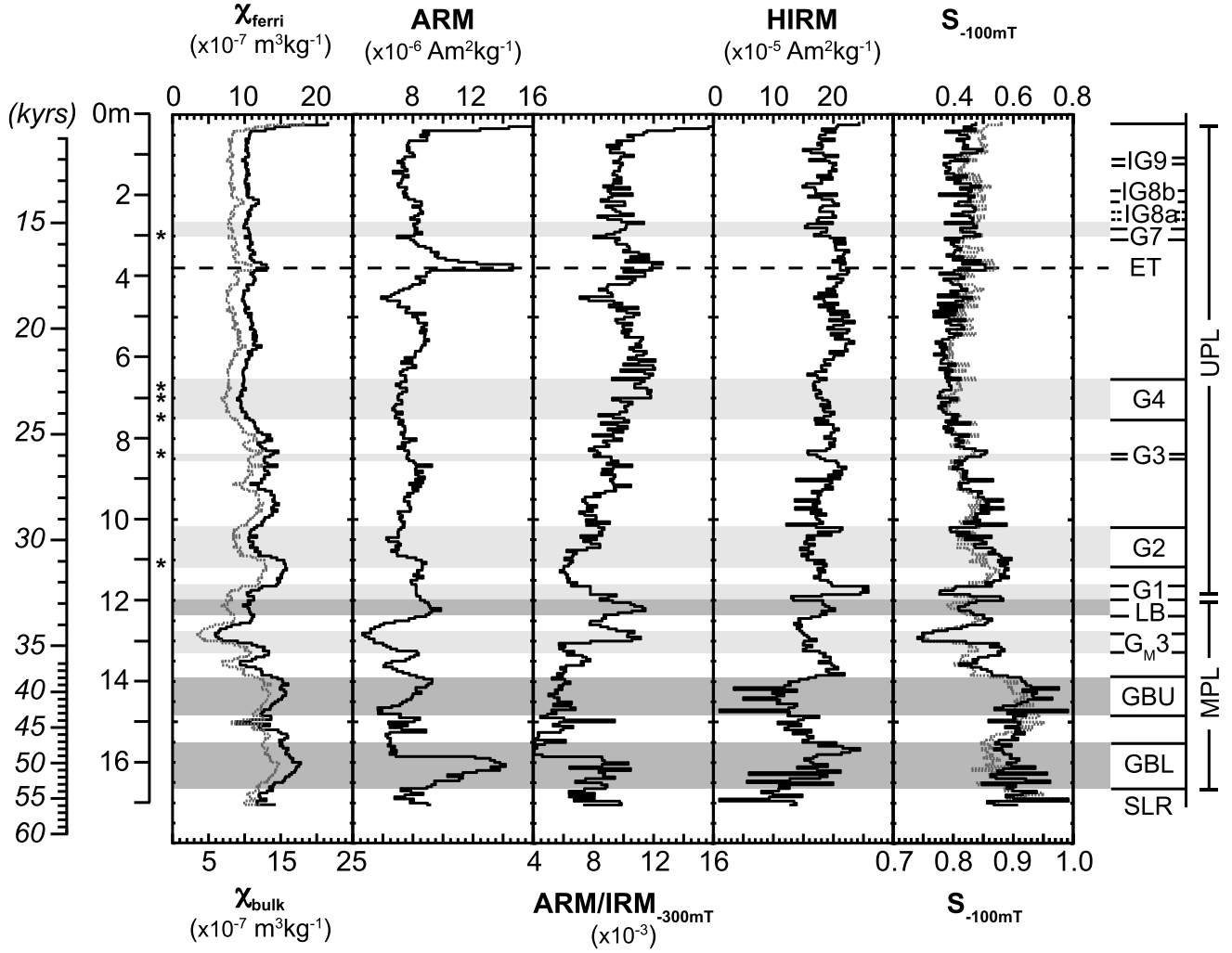

Figure 3. Bulk magnetic parameters plotted against the Nussloch P8 stratigraphy. Plots with two data sets have the parameter labeled on the upper *y* axis plotted as the dashed grey line. The light grey bands mark the tundra gley horizons, and the darker grey bands mark the palaeosols. Data for the Eltviller Tuff (ET) tephra layer found at 3.75 m are excluded. The scales of ARM and ARM/IRM$_{-300\,mT}$ have been cut off below their maximum values (~30×10^{-6} Am^2 kg^{-1} and ~0.025, respectively) for uppermost depth intervals. The stars mark the depths within Upper Pleniglacial tundra gleys where iron-oxide dissolution has been identified (see Figure 8 and section 3.1). The presented chronology is based on the age model demonstrated in Figure 2.

enhancement models found in China and in Europe [*Zhou et al*., 1990; *Maher and Thompson*, 1991; *Maher and Thompson*, 1995].

3.2. Variation With Depth of AMS Parameters

Variability in the corrected degree of anisotropy (*Pj*), shape (*Tj*), and foliation (*F*) of the AMS ellipsoids and K_{mean} of the principal axes are presented in Figure 4. The scalar mean value of *Pj* is 1.033 ± 0.011, with individual specimens ranging between 1.003 ± 0.004 (uppermost specimens, 0.7 m) and 1.067 ± 0.001 (tundra gley-palaeosol complex at ~13.5 m) (Figure 4). In general, *Pj* increases from the base of the profile toward the youngest palaeosol (LB), above which, it steadily decreases moving upward through the sequence toward the modern soil (Figure 4). The latter decrease is likely a consequence of natural compaction [*Tarling and Hrouda*, 1993]. There appears to be a positive peak in *Pj* at the base of the tundra gley unit, which decreases in a stepwise fashion, albeit with large variation, toward the top (Figure 8, less prominent in G7 and G3). In contrast for the palaeosols (LB, GBU, and GBL), there is a positive peak in *Pj* at the top surface, which systematically decreases with depth through each palaeosol layer (Figure 4). Both tundra gley and paleosol populations show higher mean values of *Pj* that the loess and total specimen

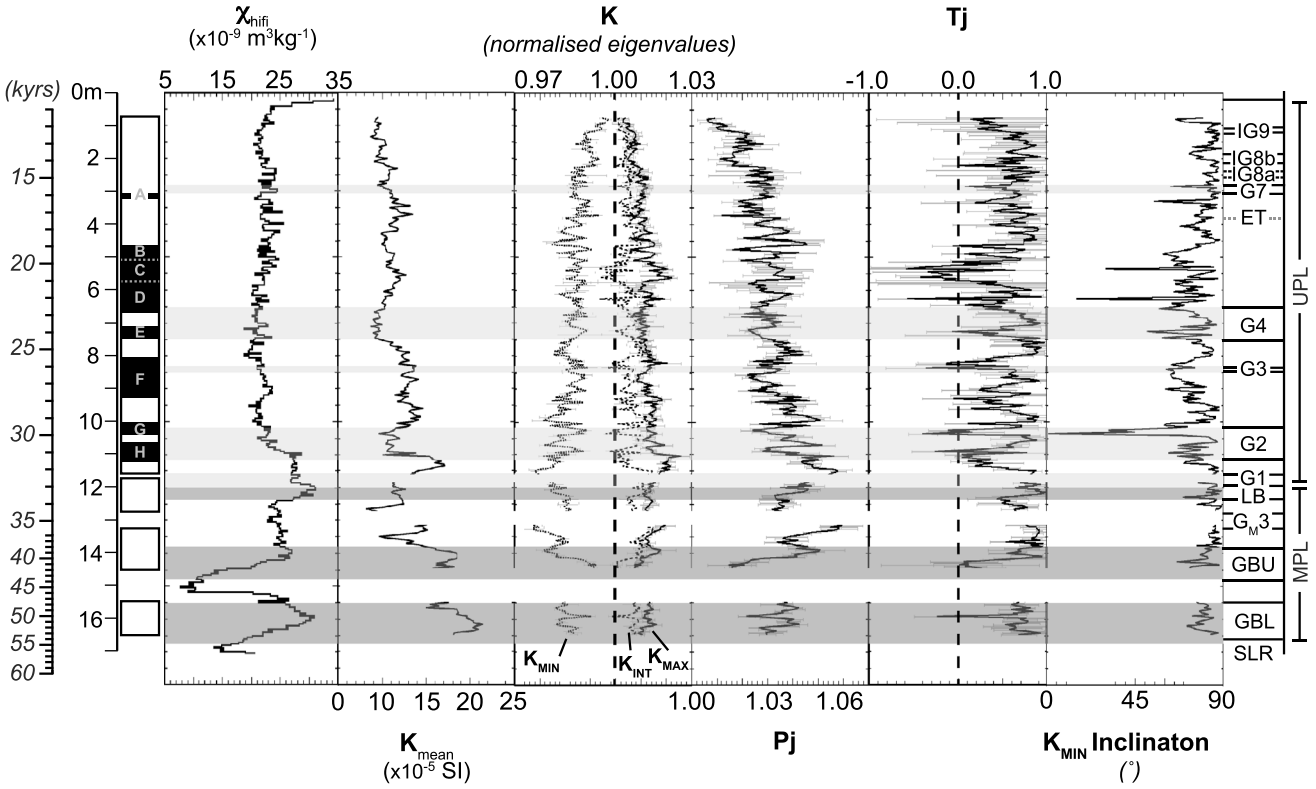

Figure 4. High-field magnetic susceptibility (χ_{hifi}), mean magnetic susceptibility (K_{mean}), and anisotropy of magnetic susceptibility (AMS) depth-averaged parameters (error bars are the standard deviation) correlated to the stratigraphy. See Figure 1 for more information on the stratigraphic profile, and see section 2 for parameter definitions. Breaks in the data are due to unsampled depths for oriented specimens; also see section 2 for explanation.

populations (Table 2). This said, the standard deviation for mean *Pj* of each stratigraphic interval overlaps, and therefore, each grouping is not strictly speaking statistically significant. The sample size *n*, of between 3 and 4 for a stratigraphic interval, is also objectively too small to render meaningful statistics.

The lack of relationship between *Pj* and K_{mean} observed in Figure 5 suggests that the AMS is controlled by the paramagnetic mineral fraction (silicates and clays) rather than ferrimagnetic (magnetite) minerals [*Borradaile*, 1987; *Rochette et al*., 1992; *Hus*, 2003]. By considering the maximum value of M_S at P8 (0.021 $Am^2 kg^{-1}$) and assuming we only have pure magnetite or pure maghemite (92 or 75 $Am^2 kg^{-1}$, respectively [*Hunt et al*., 1995]), we can calculate a maximum weight percentage between 0.023 and 0.028. By taking the average value of M_S through P8, the calculated weight percent if considering magnetite is 0.013 or maghemite is 0.016. Due to these small concentrations, it is unlikely that magnetite and/or maghemite are major contributors to the anisotropy. This is supported by the work of *Lagroix and Borradaile* [2000], who calculated that 0.1 vol % (equivalent to ~0.7–0.9 wt %) of magnetite is needed to dominate over the silicate contribution to AMS. The paleowind directions inferred from the magnetic lineation in central Alaskan loess were archived in loess having estimates of 0.3 wt % [*Lagroix and Banerjee*, 2002, 2004b]. These values are 1 order of magnitude greater than ferrimagnetic weight percent estimates in Nussloch loess.

Foliation (*F*) is strongly correlated with *P* ($r = 0.89$; Figure 5d) and on average makes up 84% of *P*. Tundra gleys and palaeosols, which have been influenced by hydromorphic processes, generally display higher mean values of *F* and *Tj* than loess specimens and the total suite of specimens (Figure 5 and Table 2), although depth trend variability makes this less convincing (Figure 4). Likewise, the standard deviation of AMS parameter means for each stratigraphic sampling interval overlap, and therefore, each grouping cannot be significantly distinguished. Lineation (*L*) does not dominate *P*, with the profile mean making up less than 25% of *P*. However, specimens with lineation-dominated anisotropy have values reaching up to 81% of *P* resulting in several excursions (around approximately 10.95 m, 10.35 m, 9.30 m, 8.30 m, 7.25 m, 6.25 m, and 5.50 m; Figure 4).

Table 2. Means and Standard Deviations of Scalar (Italics) and Tensor Averages of AMS Parameters and Axes Orientations Are Summarized[a]

Depth Range (m)	*n*	*Pj*	Pj	*Tj*	Tj	*F*	F	*L*	L	K_{MAX} Dec/Inc	K_{INT} Dec/Inc	K_{MIN} Dec/Inc	ε_{12} (deg)	ε_{23} (deg)	ε_{13} (deg)
(A) 3.35–3.30	8	*1.022 ± 0.006*	1.017 ± 0.004	*0.24 ± 0.47*	−0.08 ± 0.46	*1.013 ± 0.007*	1.008 ± 0.004	*1.008 ± 0.005*	1.009 ± 0.004	093/03	003/09	201/81	19	18	9
(B) 5.10–4.70	26	*1.027 ± 0.012*	1.023 ± 0.014	*0.25 ± 0.44*	0.53 ± 0.94	*1.017 ± 0.010*	1.017 ± 0.012	*1.009 ± 0.006*	1.005 ± 0.010	024/00	115/23	294/67	19	6	6
(C) 5.80–5.15	41	*1.038 ± 0.006*	1.027 ± 0.013	*−0.03 ± 0.40*	−0.01 ± 1.19	*1.018 ± 0.008*	1.013 ± 0.017	*1.019 ± 0.007*	1.014 ± 0.016	198/00	107/05	296/85	11	7	4
(D) 6.65–5.85	55	*1.032 ± 0.007*	1.027 ± 0.010	*0.41 ± 0.32*	0.83 ± 0.66	*1.022 ± 0.007*	1.022 ± 0.009	*1.009 ± 0.006*	1.002 ± 0.008	056/14	148/09	269/74	42	2	4
(E) 7.50–7.20	20	*1.029 ± 0.006*	1.024 ± 0.011	*0.51 ± 0.36*	0.65 ± 0.78	*1.021 ± 0.008*	1.019 ± 0.012	*1.006 ± 0.004*	1.004 ± 0.008	229/04	138/21	328/69	26	8	3
(F) 9.45–8.05	87	*1.032 ± 0.007*	1.028 ± 0.010	*0.40 ± 0.32*	0.53 ± 0.62	*1.022 ± 0.007*	1.021 ± 0.009	*1.009 ± 0.058*	1.006 ± 0.015	052/00	143/16	322/74	8	3	2
(G) 10.40–10.05	24	*1.035 ± 0.009*	1.030 ± 0.012	*0.28 ± 0.40*	0.34 ± 0.78	*1.022 ± 0.011*	1.020 ± 0.014	*1.011 ± 0.005*	1.010 ± 0.010	244/04	152/30	340/60	9	7	5
(H) 11.25–10.65	39	*1.042 ± 0.010*	1.040 ± 0.012	*0.31 ± 0.32*	0.36 ± 0.49	*1.027 ± 0.009*	1.027 ± 0.010	*1.014 ± 0.007*	1.013 ± 0.010	212/09	120/14	334/74	6	3	3
Loess	**523**	***1.031 ± 0.011***	**1.027 ± 0.013**	***0.43 ± 0.36***	**0.70 ± 0.74**	***1.021 ± 0.009***	**1.021 ± 0.011**	***1.008 ± 0.006***	**1.004 ± 0.009**	**049/02**	**140/07**	**300/83**	**7**	**1**	**1**
Tundra gleys	**206**	***1.037 ± 0.010***	**1.033 ± 0.013**	***0.55 ± 0.31***	**0.73 ± 0.62**	***1.027 ± 0.009***	**1.027 ± 0.012**	***1.007 ± 0.005***	**1.004 ± 0.010**	**231/02**	**141/10**	**330/80**	**8**	**1**	**1**
Palaeosols	**134**	***1.036 ± 0.009***	**1.033 ± 0.012**	***0.56 ± 0.31***	**0.84 ± 0.54**	***1.027 ± 0.009***	**1.027 ± 0.011**	***1.007 ± 0.004***	**1.002 ± 0.008**	**070/02**	**161/07**	**328/83**	**14**	**1**	**1**
Primary fabric	**396**	***1.031 ± 0.012***	**1.029 ± 0.013**	***0.56 ± 0.28***	**0.80 ± 0.63**	***1.023 ± 0.010***	**1.023 ± 0.010**	***1.006 ± 0.004***	**1.003 ± 0.008**	**069/03**	**157/03**	**293/86**	**6**	**1**	**1**
Total	**863**	***1.033 ± 0.011***	**1.029 ± 0.014**	***0.48 ± 0.34***	**0.75 ± 0.70**	***1.023 ± 0.010***	**1.024 ± 0.012**	***1.008 ± 0.006***	**1.003 ± 0.009**	**053/01**	**143/07**	**315/83**	**5**	**1**	**1**

[a]The considered populations are the eight identified reworked intervals (A–H), all specimens located within identified primary AMS depth intervals; all specimen stratigraphically constrained within loess, tundra gley, or paleosol depth intervals; and finally the total suite of specimens.

3.3. AMS Orientation Distributions

The AMS orientation distribution of the entire population of specimens of the P8 sequence (Figure 6) displays a nearly vertical minimum susceptibility axis (K_{MIN}) with a tensor mean orientation of 315/83 and ε_{13} of 1° (see Table 2). Intermediate and maximum axes (K_{INT} and K_{MAX}) are horizontal with tensor mean orientations of 143/07 and 053/01, respectively, and ε_{12} of 5° (Table 2). The orientation distribution defines an oblate magnetic fabric with a foliation plane gently dipping (7°) to the SE and a well-defined horizontal lineation directed in the NE-SW direction. Primary sedimentary depositional processes, including aeolian deposition, lead to oblate magnetic fabrics with foliation planes parallel to slightly imbricated to the depositional bedding plane. The orientation distributions of isolated populations of loess, tundra gley, and other paleosol specimens yield tensor mean orientations of the three principal axes that are not statistically significant from the entire specimen suites (Figure 6 and Table 2). There is one noteworthy exception, the K_{min} tensor mean orientation of the tundra gley specimen population plunges 80° instead of 83° for the total population of specimens and loess or paleosol populations. Since the ε_{13} value is 1° for all four populations, the slightly greater dipping (10° instead of 7°) magnetic foliation plane of the tundra gley specimen population is statistically significantly different.

As mentioned, the palaeosol subpopulation does not show significant variations away from the loess or total specimen populations in its orientation distribution. However, it does show an ε_{12} of 14°, double the value of the loess and tundra gley subpopulations, suggesting that the orientation between K_{MAX} and K_{INT} is less well defined. A more scattered distribution is also observed between 14.50 and 14.15 m (GBU), but the orientation distribution of the specimens within does not differ significantly from the other palaeosol populations.

The subpopulations presented above and in Figure 6 were delimited by the stratigraphic unit boundaries identified in the field during sampling (Figure 1). *Taylor and Lagroix* [2014] demonstrated that the environmental imprints left on the mineral magnetic record were not necessarily confined to the stratigraphic unit. For example, dissolution of ferrimagnetic particles driven by redoxomorphic processes was sometimes observed outside of gley tundra units. Redoxomorphic features are one of the criteria used in the field to delimit tundra gley

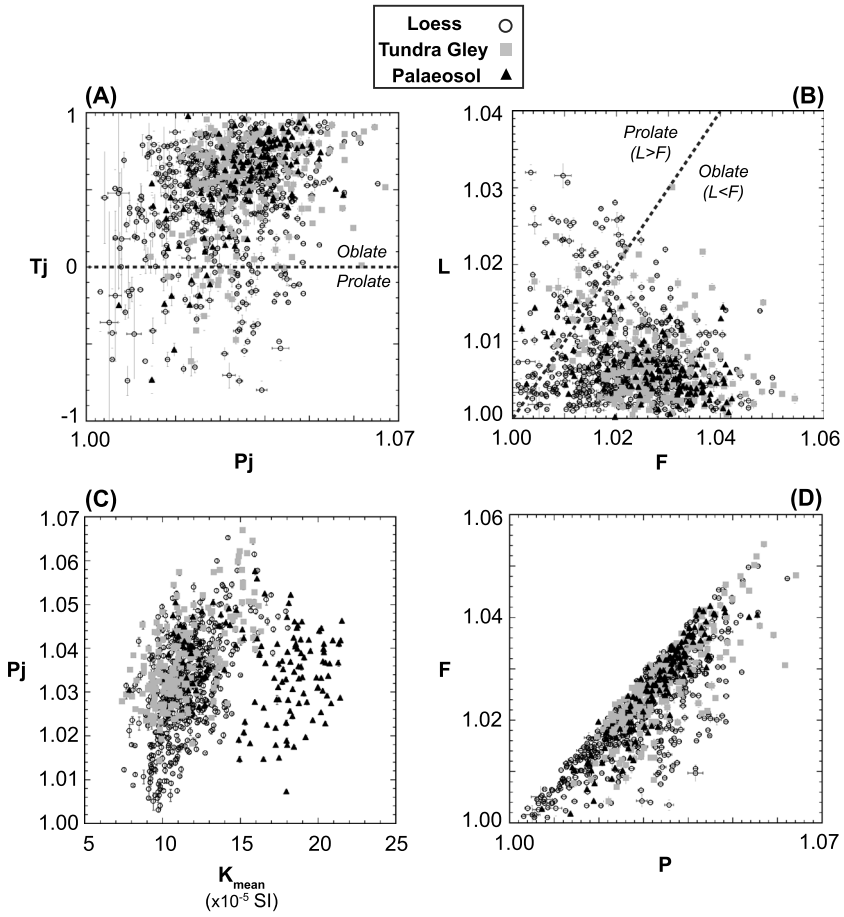

Figure 5. Biplots of AMS parameters for each stratigraphic type: (a) corrected degree of anisotropy (P_j) versus the shape parameter (T_j) [*Jelinek*, 1981]. Most of the samples fall into the oblate section, expected for aeolian sediments. Samples with low anisotropy have large T_j error ranges, showing that below 1% anisotropy, the shape of the AMS ellipsoid is poorly defined. (b) Foliation (F) versus lineation (L) Flinn diagram [*Flinn*, 1962]. (c) Mean magnetic susceptibility (K_{mean}) against P_j. (Note that the Eltviller Tephra samples are not plotted.) (d) P versus F.

horizons [*Antoine et al*., 2001, 2002, 2009]. It can therefore be concluded that sediment reworking related to the development of redoxomorphic features may affect parts of the deposit outside the stratigraphic boundaries defined for tundra gley horizons. Eight depth intervals (Figure 7 and Table 2) have been identified as having orientation distributions that significantly depart from that described previously.

A (3.35–3.30 m, 10 cm thick) located in a thin layer just below tundra gley G7 displays a prolate orientation distribution with less well defined lineation ($\varepsilon_{12} = 19°$) and low tensor mean value of *Pj*. Values of *Tj* for individual specimens are a mix of prolate and weakly oblate.

B (5.10–4.70 m, 40 cm) is found in laminated loess layers (marked by thin laminations and cryodessication microcracks, a sandy/cakey texture observed in the field between 5.00 and 4.80 m), where incipient tundra gley horizons are weakly observed. This interval displays an oblate orientation distribution with dipping foliation plane to the ESE by 23° and less well defined horizontal lineation NNE-SSW oriented. The upper and lower depth boundaries of this interval are marked by relative lows in *Pj*, with a relative high over central depths. Individual specimens show an oblate fabric, with increased values in *Tj* compared with the underlying unit.

C (5.80–5.15 m, 65 cm) is within a laminated loess interval, displaying a weakly prolate orientation distribution, where individual specimens show *Tj* values < 0. The foliation plane is shallowly dipping (5°) in an ESE direction. The calculated tensor mean anisotropy is dominated by the lineation component, and there is an overall high in *Pj*.

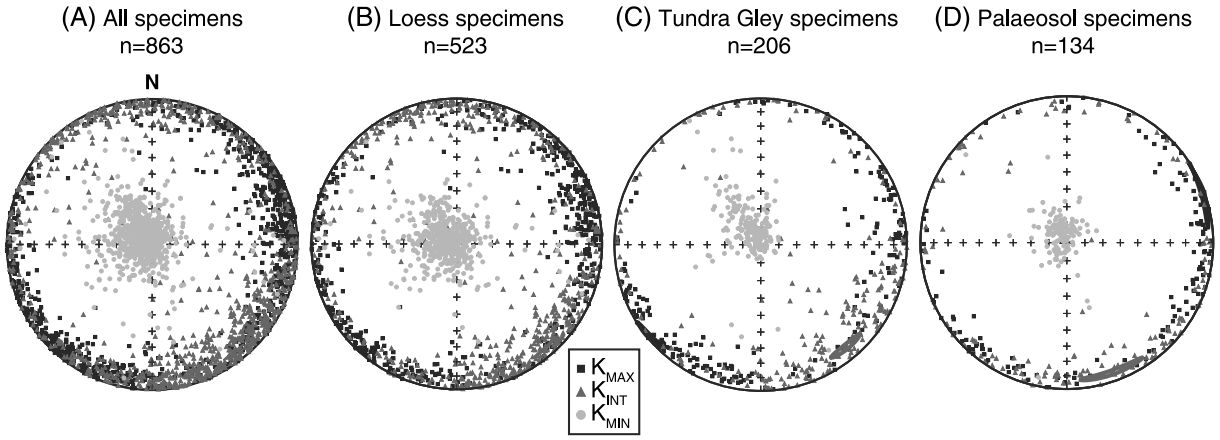

Figure 6. Lower hemisphere equal area stereoplots of (a) all Nussloch P8 specimens, (b) loess, (c) main tundra gleys (G2–G7; G1 and G_M3 were not sampled), and (d) palaeosols (GBL, GBU, and LB). Tensor mean values are listed in Table 2.

D (6.65–5.85 m, 80 cm) is located in the same loess unit as C with its base in the upper limits of tundra gley G4. It shows an oblate orientation distribution with gently (9°) dipping foliation to the SE. K_{MAX} and K_{INT} are isotropically distributed within the foliation plane (ε_{12} of 42°). Individual specimens display oblate fabrics, with an exception at 6.25 m (and slightly at 6.45 m). *Pj* shows a high between 6.30 and 6.10 m, and while individual specimens between 6.10 and 5.85 show a broad low in *Pj*, they have much larger variability.

E (7.50–7.20 m, 30 cm) is found at the base of tundra gley G4 (oxidized layers were observed in the field at 7.35–7.30 m), displaying an oblate orientation distribution with a foliation plane dipping 21° to the SE and a weakly defined ($\varepsilon_{12} = 26°$) horizontal lineation oriented SW-NE. Specimens display lower values of *Pj* and show less oblate fabrics compared to the surrounding units, with *Tj* close to 0 (large standard deviations) specifically over the 7.35–7.20 m depth interval.

F (9.45–8.05 m, 140 cm) is a thick grouping within a laminated loess interval that includes tundra gley G3. It displays an oblate orientation distribution with a foliation plane dipping 16° to the SE and a horizontal lineation in an ENE-WSW direction. The dispersed points mark random specimens throughout the interval. Individual specimens show prolate fabrics ($Tj < 0$) between 8.40 and 8.15 m and weakly oblate fabrics ($Tj < 0.2$) between 9.45 and 9.05 m, both coinciding with superimposed highs in *Pj* (also at 8.90–8.80). Overall, there is lower *Pj* in this interval compared with the surrounding loess.

G (10.40–10.05 m, 35 cm) is located in the transition from tundra gley G2 to the overlying loess and shows an oblate orientation distribution with well-defined principal axes. It has a dipping (30°) foliation to the SSE and horizontal lineation in a WSW-ENE direction. Individual samples display prolate fabrics (with high *Pj*) at the boundaries of this interval and an oblate shape between 10.20 and 10.10 m.

H (11.25–10.65 m, 60 cm) is situated in the bottom half of tundra gley G2 (red banding/oxidation marks were observed around 11.25–11.00 m). This interval is characterized by a prolate-oblate orientation distribution with high tensor mean values of *Pj*. For individual samples between 11.25 and 10.90, where dissolution has been observed, values of *Tj* are more prolate and show higher values of *Pj*. There is also a relative high in *Pj* between 10.75 and 10.65.

In summary, the above eight groupings (A–H) represent 4.60 m of cumulated depth or 27% of the profile depth. They display either prolate orientation distributions or oblate orientation distributions with magnetic foliation planes dipping by 9–30° and showing dip directions transitioning from the SSE to the ESE as we move upprofile. These depth intervals have undergone reworking after their initial wind deposition and are discussed in the following section 4.1.

The AMS orientation distributions outside of the aforementioned eight groupings display a horizontal magnetic foliation and near-vertical K_{MIN}. At a population level, the magnetic lineation is well defined ($\varepsilon_{12} = 6°$) and has an ENE-WSW direction. Paleosol intervals are assumed to not retain the original aeolian depositional mineral fabric. Therefore, outside of the eight groupings and the palaeosol horizons

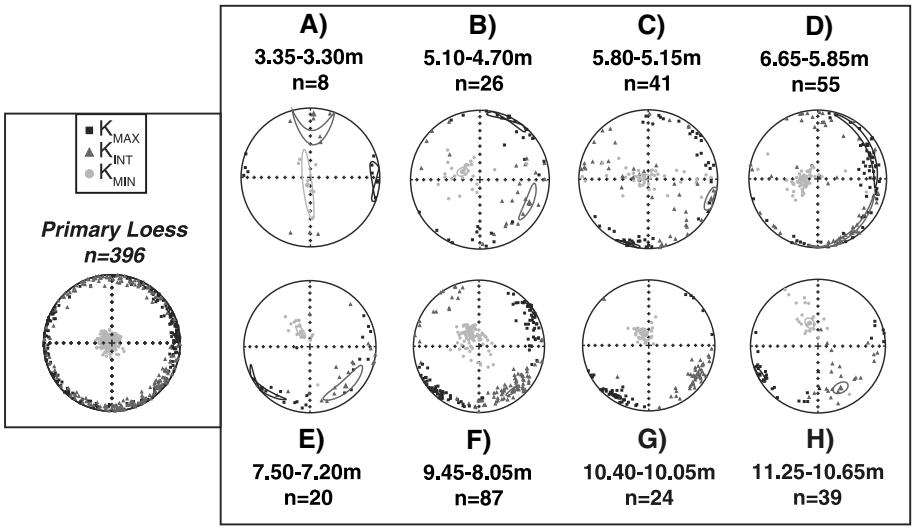

Figure 7. Lower hemisphere equal area stereoplots of the AMS principal axes and their 95% confidence ellipses. (left) All specimens within intervals displaying primary aeolian magnetic fabrics and (right) eight intervals interpreted as having secondary magnetic fabrics. These all show either prolate orientation distributions (A, C, and H) or oblate orientation distributions with dipping magnetic foliation planes (B, D, E, F, and G).

(discussed in section 4.2), the orientation distributions are interpreted as primary aeolian magnetic fabrics (further discussed in section 4.3) and represent 6.45 m of cumulated depth or 38% of the profile depth.

4. Discussion

4.1. Secondary Magnetic Fabrics

The intervals A–H between 11.5 and 3.3 m (~32–16 ka) have experienced postdepositional reworking. Based on the model by *Antoine et al.* [2009], these intervals have an age of ~30–22 ka. Across western Europe, this period corresponds to the Upper Pleniglacial, the coldest period of the Weichselian, and is marked by ice advance, widespread permafrost, and significant aeolian dust deposition [e.g., *Vliet-Lanoë*, 1989; *Vandenberghe and Pissart*, 1993; *Vandenberghe et al.*, 1998; *Antoine et al.*, 2001; *Guiter et al.*, 2003; *Antoine et al.*, 2009]. It is strongly indicated that permafrost was present in western Europe during the period between around 30 and 20 ka from evidence of residual permafrost tables and well-developed ice wedges [e.g., *Vliet-Lanoë*, 1989, 1991; *Vandenberghe and Pissart*, 1993; *Vandenberghe et al.*, 1998; *Antoine et al.*, 1999, 2001; *Vandenberghe and Nugteren*, 2001]. Although such features have not been observed in Nussloch P8, there are various other pieces of evidence in the field for the occurrence of permafrost. As with the other Nussloch profiles [*Antoine et al.*, 2001, 2002, 2009], the presence of tundra gley horizons and their associated cryoturbation (i.e., major: G2, G3, and G4 and incipient: units 30 and 33), cryodessication microcracks in laminated loess layers (units 32, 29, 27, and 24 found between 10.2 m and 4.8 m) and gelifluction have been observed. Moreover, a large "regressive thermokarst" infilling was observed at the Nussloch P1 site [*Antoine et al.*, 2001]. The fact that large ice wedges found elsewhere in permafrost environments throughout western Europe appear absent at Nussloch may be the result of lower precipitation, very thick snow cover, or the location of the site on top of a greda topography [*Moine et al.*, 2008]. Mean annual paleoprecipitation obtained by *Hatté and Guiot* [2005] from inverse modeling of carbon-13 isotope data was estimated to be stable throughout the 28–17 kyr period at approximately 280 mm/yr, which is 3 to 4 times less than present-day values. Prior to this period, paleoprecitation appears more variable with up to 200 mm/yr oscillations. The above is in agreement with a compilation of studies in Europe presented by *Huijzer and Vandenberghe* [1998], showing a general increasing aridity toward the Last Glacial Maximum.

Two important field-observed sedimentary features linked to permafrost-related and cryogenic processes occur frequently over depths encompassing reworked intervals A–H. First, intervals A, E, G, and H are found within or close to tundra gley horizons. Second, intervals B, C, D, and F are found exclusively in laminated loess layers. Therefore, we can postulate a link between these reworked intervals characterized

by secondary AMS magnetic fabrics and processes leading to the redoxomorphic features (hereafter referred to as gleying) observed in tundra gley horizons and to the lamination of loess.

4.1.1. Tundra Gley Horizons

Gleying can modify the mineral magnetic assemblage through recurring dissolution and reprecipitation of iron oxides/oxyhydroxides [e.g., *Taylor and Lagroix*, 2014]. Onset of gleying is associated with rapid warming events during glacial/stadial periods and is perhaps penecontemporaneous with warm phases of Dansgaard-Oescheger events [*Rousseau et al*., 2007; *Moine et al*., 2008; *Antoine et al*., 2009]. An increase in relative frequency of hydrophilous land molluscs (*Succinea Oblonga*) indicates that the climate was relatively cool and moister for the development of the thickest tundra gley horizons (i.e., G2 and G4 in P8) [*Moine et al*., 2008] and both colder and dryer upsection. Repeated warming events and increased humidity would initiate degradation of permafrost (increasing active layer thickness between the surface and the top of the permafrost zone), invoke cryoturbation, and allow the infiltration of water. Considering the porous nature of loess and any root tracks for example, percolating water can travel toward the impermeable permafrost boundary. Here at this barrier, water may stagnate or continue to percolate down the top surface boundary of the permafrost zone and in both cases induce sediment remobilization (gelifluction) over the frozen ground [*French*, 1988]. These short periods of climatic improvement can also initiate the local development of thermokarst processes (permafrost melting). Each major tundra gley in Nussloch is characterized by cryoturbation with some having gelifluction features at the surface [*Antoine et al*., 2001, 2009].

It has been previously shown for the P4 sequence that discrete depth intervals associated with tundra gley horizons display a decrease in the concentration of fine-grained magnetite due to dissolution and postulated to result from stagnation of water [*Taylor and Lagroix*, 2014]. Following the combination of observations established in *Taylor and Lagroix* [2014] to identify intervals of iron oxide dissolution, six intervals having likely undergone dissolution are identified along the P8 sequence (Figures 3 and 8 and section 3.1). The dissolution is apparent from the contradicting observations of decreasing ferrimagnetic concentration with increasing ferrimagnetic grain size (Figure 8 and section 3.1) over an interval associated to a period of relative climate amelioration, where weaker wind strength slowed sediment accumulation permitting the development of immature soils (tundra gley horizon). The dissolution depth intervals show higher *Pj* values and more oblate AMS ellipsoids (Figure 8). Increased pore water content needed for dissolution would also logically lead to particle remobilization increasing the degree of mineral alignment and increasing *Pj*. The oscillation of *Pj* through the two thickest tundra gley horizons (G4 and G2) could be highlighting multiple stages of degradation, overprints of movement in the permafrost table (and thus the zone of dissolution and reorientation of minerals), and/or seasonal movement at the surface of the active layer. On the other hand, the observed minimum in *Pj* at the upper boundary of most tundra gley horizon is likely due to bioturbation. Increased abundances of mollusc shells, burrows, and roots at the top of tundra gley horizons are evidence of increased biological activity [*Moine et al*., 2008; *Antoine et al*., 2009]. In addition to the biological activity, the upward movement of sediment due to negative frost susceptibility gradient [e.g., *Vliet-Lanoë*, 1991; *Huijzer*, 1993] would also decrease in *Pj*.

The AMS orientation distributions of G2, G3, and G4 (the oldest UPL tundra gley horizon G1 was unfortunately not sampled) are oblate and show dipping magnetic foliation planes similar to the associated reworked intervals G and H, F, and D and E, respectively, displaying 16°–30° dips of their magnetic foliation planes (Figure 8 and Table 2). Moreover, G2, G3, and G4 also contain five of the six identified dissolution bands. Together, they provide evidence of increased pore water enabling particle remobilization in stagnating water or percolating water environments. To explain both the dissolution of iron oxides and the observed dipping foliation, we present the following scenario. At the interface between a horizontal permafrost layer and the overlying sediment (i.e., the active layer), water stagnates and provides an avenue for both efficient grain orientation and iron oxide dissolution. By introducing a sloping permafrost boundary, water will continue to percolate downslope and still allow grain reorientation and provide an avenue for the generation of dipping magnetic foliation planes. However, this would not favor water stagnation (and so iron oxide dissolution). A certain amount of roughness of the permafrost surface is likely and would lead to local areas of water stagnation and water percolation to coexist. Conversely, the AMS orientation distributions of tundra gley horizon upprofile (G7 < 18 ka; Figure 8) are indistinguishable from that of primary loess magnetic fabrics. This corroborates with environmental magnetism results of weakening

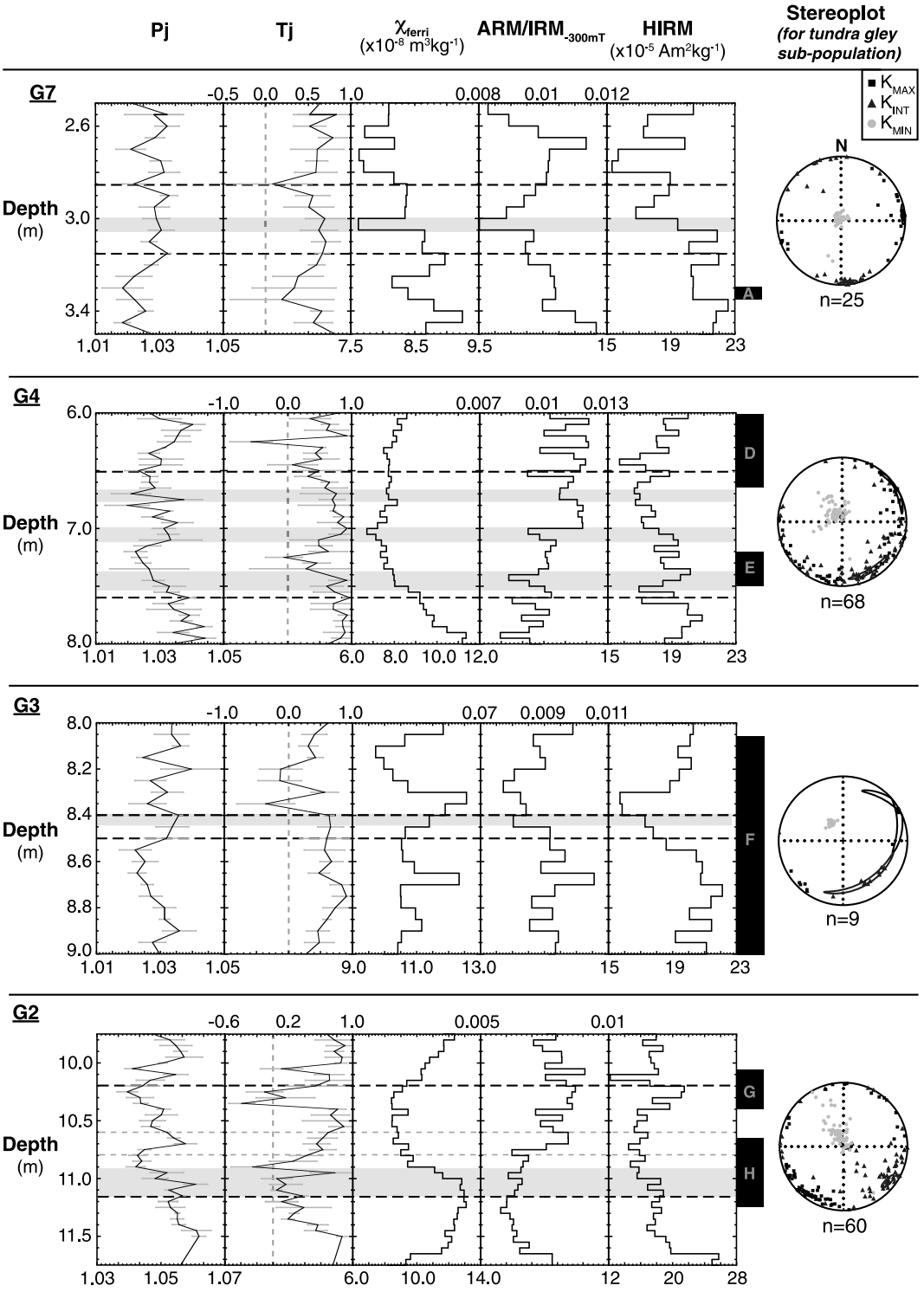

Figure 8. Selection of AMS parameters and bulk magnetic parameters for Upper Pleniglacial tundra gley horizons (G2, G3, G4, and G7) and surrounding loess. Each stereoplot represents the population of the adjacent tundra gley stratigraphic unit only. The dashed lines mark the upper and lower boundaries of tundra gley horizons as identified in the field. (Note that G2 is twofold, where the lighter dashed lines mark internal tundra gley boundaries.) The shaded bands mark the intervals over which redoxomorphic processes induced by waterlogging have left an imprint on the magnetic record (using the same principals exposed in *Taylor and Lagroix* [2014]. The lettered boxes displayed on the right axis of the HIRM plots refer to the reworked intervals of Figure 7.

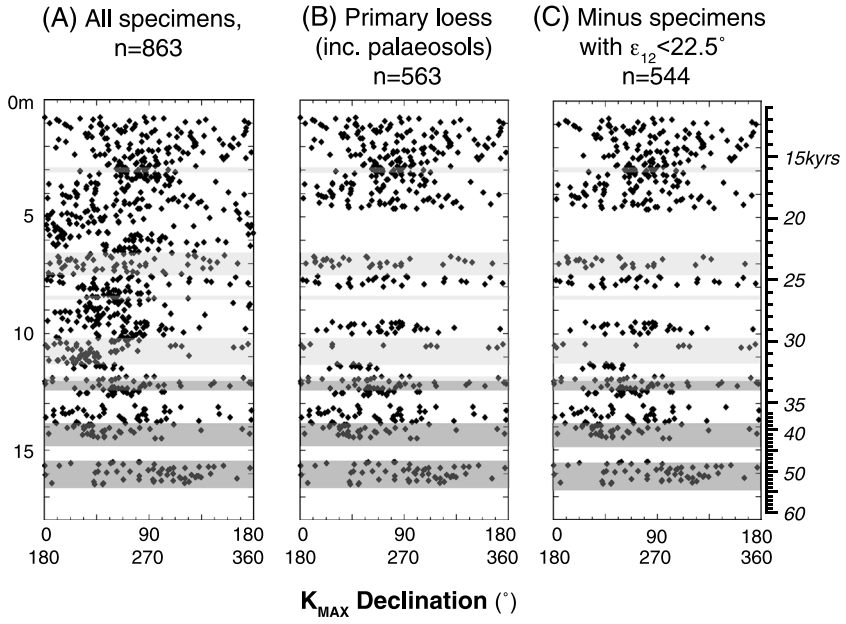

Figure 9. Declination of K_{MAX} principal axes with depth and progressive data reduction from (a) full data set, (b) minus intervals showing a secondary fabric, and (c) isolation of the most significant orientations with samples showing 95% confidence ellipse half-angle uncertainty between K_{MAX} and K_{INT} (ε_{12}) less than 22.5°. The shaded bars represent the stratigraphy (see Figures 1 and 3 for nomenclature).

gley-induced diagenesis upsection [*Taylor and Lagroix*, 2014]. These upper tundra gley horizons represent periods of time where climate improvement is less significant and of greater aridity compared to those downprofile.

4.1.2. Laminated Loess Layers

Laminated loess layers are described as "superimposed fining upward microsequences" from fine sand to silt [*Antoine et al*., 2001] intercalated with cryodesiccation microcracks that have niveo-aeolian characteristics [*Antoine et al*., 2001, 2009]. These laminated layers are postulated to form during short climatic events with successions of cold fronts [*Antoine et al*., 2009; *Moine*, 2014], in which the observed freeze-thaw fabric indicates that seasonal freezing accompanied their accumulation [*Antoine et al*., 2001; *Moine et al*., 2008]. Loess is known to be a poorly sorted material, unlike coarser aolian sands [*Muhs et al*., 2014]. The upward fining laminations may originate from deposition of loess onto a snow-covered ground and larger particles settling out first during snowmelt. Experimental modeling found that intercalation of snow during sedimentation does not always induce laminated structures [*Dijkmans and Mücher*, 1989], but here intercalated with cryodessication cracks, it seems to be probable origin. The laminations themselves have horizontal intersection lineations on the cleaned vertical sampling face, which strikes approximately in the NW to SE direction. The probability of these being truly horizontal in three-dimensional space is very high since only a depositional surface with a dip direction orthogonal to the cleaned surface strike can falsify our assumption. The foliation planes of reworked intervals B (23° dip ESE), C (5° dip ESE), D (16° dip E), and F (16° dip SE) which occur in close association with horizontally laminated loess layers archive the attitude of different surfaces. The latter records the top surface of the deposit in direct contact with the atmosphere while the former, most probably records the attitude of the permafrost surface. The increase in pore water necessary for grain remobilization may have come from snowmelt. As mentioned above, other proxies characterize the periods of rapid loess deposition and climate conditions upprofile as increasingly colder and drier. If snowmelt was the leading source of precipitation, this limited source of available water able to percolate down to the permafrost zone would have been concentrated over a relatively short snowpack melting window. This is consistent with the lack of redoxomorphic features observed in association with reworked intervals B, C, D, and F (excluding tundra gley G3). Highly scattered AMS axes of reworked interval B may in addition reflect grain remobilization due to frost heaving. Loess material is predominantly silty and therefore extremely susceptible to frost heave and cryoturbation

[*French*, 2007]. Since there are few examples of such scattering at Nussloch, one may question the ubiquity of frost heaving or more pertinently in our opinion the effects of frost heaving on loess. Perhaps the response on the magnetic fabric is dependent on pore water content.

4.2. Effects of Pedogenesis on AMS

The destruction of primary fabric (and a decrease in the degree of anisotropy) due to pedogenesis has been observed in various studies on loess deposits [e.g., *Mathé et al*., 1997, 1999]. More isotropic fabric and lower values of *Pj* due to increased biological activity (and potentially the in situ formation of iron oxides) in pedogenically altered loess [e.g., *Matasova et al*., 2001] may therefore be expected. However, the three palaeosols found at the base of P8 (LB, GBU, and GBL) display AMS orientation distributions and AMS ellipsoid parameters statistically identical to those of primary loess fabric (Figure 6 and Table 1). LB, GBU, and GBL are classified as arctic brown soils or cambisols, suggesting that they had not develop into very mature soils due to restricted water availability [*Ellis and Mellor*, 1995], leading to little overprinting of the primary magnetic fabric. The peak in *Pj* at the top surface of the palaeosols is likely a result of surface processes such as runoff. The slight decreasing trend of *Pj* with depth (Figure 5) could be reflecting the aggradation of the soil horizon, where bioturbation is more efficient in randomizing grain orientation.

4.3. Primary Magnetic Fabrics

The unaltered, primary fabric of loess intervals at Nussloch are characterized by horizontal magnetic foliation and at a population level, a well-defined magnetic lineation in the ENE-WSW orientation (Figure 7). Marking this as a possible preferred orientation due to a dominant wind direction, there would not be an agreement with the hypothesis of dust transport from the English Channel and Northern France [e.g., *Rousseau et al*., 2007; *Antoine et al*., 2009; *Sima et al*., 2009]. However, as the loess grain size at Nussloch tends toward very coarse silt, a more dominant local source of material could be arising from the braided alluvial plains of the Rhine [*Antoine et al*., 2009]. A directional preference would arise from the preferred alignment of ferrimagnetic magnetite (and maghemite) which has an intrinsically prolate AMS controlled by its grain shape. Given the low concentration of ferrimagnetic minerals found in this sequence, a magnetic lineation is unlikely to significantly express itself on top of the dominant paramagnetism-dominated magnetic foliation as argued in section 3.2. The variation with depth of the most significant magnetic lineation within intervals having archived primary magnetic fabrics reveals fairly high scatter between specimens of a single sampling depth (Figure 9). This also does not transpire confidence in isolating a meaningful paleowind direction. This said, there is one note worthy observation: the tightly grouped magnetic lineation directed in a NE-SW orientation observed in loess specimens of unit 22 (~33–32 ka) wedged in between G1 and G2. This loess unit is temporally coeval to loess unit 4 (33.0 ± 2.1 ka) at Havrincourt in Northern France from which a significant magnetic lineation was recovered from an apparent primary aeolian magnetic fabric [*Antoine et al*., 2014]. The inferred dominant paleowind direction there was orientated NNE to SSW, which is coincidentally very close to the magnetic lineation recovered in unit 22 at P8. This said, at the present time, we maintain that from such low concentration of magnetite (<0.03 wt %), paleowind directions cannot reliably be inferred. Therefore, the interpretation of past wind-transporting dominant directions from Nussloch sequences is highly speculative.

5. Conclusions

This anisotropy of magnetic susceptibility study has provided an insight into depositional and postdepositional processes that occurred during the last glacial period (~56–12 ka) at Nussloch. First, postdepositional deformation is identified within intervals having AMS orientation distributions that are prolate or oblate with magnetic foliation planes dipping as much as 30°. These magnetic fabrics are due to processes associated with seasonal changes in permafrost/active layer dynamics and influenced by variation in water availability, which is greatest at the base of sequence and becomes more limited upprofile. Given the observation that tundra gley horizons upprofile (<20 ka; G7, incipient tundra gleys IG8 and IG9) are characterized by AMS orientation distributions and AMS parameters similar to those of primary magnetic fabrics, reduced amounts of available water and lower intensity of gleying processes limit overprinting of the primary depositional magnetic fabrics. Primary fabrics, on the other hand, are defined by near-vertical K_{MIN} axes and horizontal magnetic foliations, which are expected for silt-size sediment deposition onto a horizontal bedding plane. Primary aeolian sedimentary magnetic fabrics are

observed between 12.65–12.4 m, 12.05–11.30 m, 10.30–9.5 m, 8.00–7.55 m, 7.45–6.70 m, 4.65–3.40 m, and 3.25–0.70 m. The ferrimagnetic content estimated in these intervals is between 0.02 and 0.03 wt %. Such concentrations, in comparing to studies where significant magnetic lineations were interpreted as paleowind directions, are 1 order of magnitude lower. Therefore, defining palaeowind directions from primary magnetic fabrics from Nussloch sequences would be highly speculative. Finally, pedogenesis, leading to the formation of the Middle Pleniglacial paleosols at Nussloch, has not played an important role in modifying the aeolian depositional magnetic fabric.

Acknowledgments
The data for this paper can be made available upon request. This work was supported through ANR-08-BLANC-0227-CSD6 and CNRS-INSU SYSTER research grants. Magnetic measurements were carried out in IPGP's paleomagnetic laboratory and benefitted from the IPGP-IMPMC Mineral Magnetism Analytical Platform financed by Region Ile-de-France, UPMC, IPGP, CNRS-INSU, and ANR. We would like to thank the ACTES team (Denis-Didier Rousseau, Pierre Antoine, Olivier Moine, Christine Hatté, and Caroline Gauthier), Jessica Till, and Manfred Loescher for their help. We also wish to thank M. Dekkers (Associate Editor), S. Spassov, and an anonymous reviewer for their helpful and constructive comments. This is IPGP contribution 3620.

References

Antoine, P., D. D. Rousseau, J. P. Lautridou, and C. Hatté (1999), Last interglacial-glacial climatic cycle in loess-palaeosol successions of north-western France, *Boreas*, *28*(4), 551–563.
Antoine, P., D. D. Rousseau, L. Zöller, A. Lang, A. V. Munaut, C. Hatté, and M. Fontugne (2001), High-resolution record of the last interglacial-glacial cycle in the Nussloch loess-palaeosol sequences, Upper Rhine Area, Germany, *Quat. Int.*, *76*(77), 211–229.
Antoine, P., D. D. Rousseau, C. Hatté, L. Zöller, A. Lang, M. Fontugne, and O. Moine (2002), Événements éoliens rapides en contexte loessique: L'exemple de la séquence du Pléniglaciaire supérieur weichselien de Nussloch (Vallée du Rhin-Allemagne), *Quaternaire*, *13*(3–4), 199–208.
Antoine, P., D. D. Rousseau, O. Moine, S. Kunesch, C. Hatté, A. Lang, H. Tissoux, and L. Zöller (2009), Rapid and cyclic aeolian deposition during the Last Glacial in European loess: A high-resolution record from Nussloch, Germany, *Quat. Sci. Rev.*, *28*, 2955–2973.
Antoine, P., et al. (2014), Les séquences loessiques Pleistocene Supérieur d'Havrincourt (Pas-de-Calais, France): Stratigraphie, paleoenvironnements, géochronologie et occupations Paléolithiques, *Quaternaire*, *25*(4), 321–368.
Bibus, E., M. Frechen, M. Kösel, and W. Rähle (2007), Das jungpleistozäne Lößprofil von Nußloch (SW-Wand) im Aufschluss der Heidelberger Zement AG, *Eiszeitalter Ggw.*, *56*, 227–255.
Borradaile, G. (1987), Anisotropy of magnetic susceptibility: Rock composition versus strain, *Tectonophysics*, *138*(2), 327–329.
Borradaile, G. J., and B. Henry (1997), Tectonic applications of magnetic susceptibility and its anisotropy, *Earth Sci. Rev.*, *42*(1), 49–93.
Borradaile, G. J., and M. Jackson (2010), Structural geology, petrofabrics and magnetic fabrics (AMS, AARM, AIRM), *J. Struct. Geol.*, *32*(10), 1519–1551.
Bradák, B. (2009), Application of anisotropy of magnetic susceptibility (AMS) for the determination of paleo-wind directions and paleo-environment during the accumulation period of Bag Tephra, Hungary, *Quat. Int.*, *198*(1), 77–84.
Cogné, J. P. (2003), PaleoMac: A Macintosh™ application for treating paleomagnetic data and making plate reconstructions, *Geochem. Geophys. Geosyst.*, *4*(1), 1007, doi:10.1029/2001GC000227.
Dijkmans, J. W. A., and H. J. Mücher (1989), Niveo-aeolian sedimentation of loess and sand: An experimental and micromorphological approach, *Earth Surf. Processes Landforms*, *14*(4), 303–315.
Ellis, S., and A. Mellor (1995), *Soils and Environment*, Routledge, New York..
Flinn, D. (1962), On folding during three dimensional progressive deformation, *Q. J. Geol. Soc. London*, *188*, 385–428.
French, H. M. (1988), Active layer processes, in *Advances in Periglacial Geomorphology*, pp. 151–177, John Wiley, New York.
French, H. M. (2007), *The Periglacial Environment*, 3rd ed., John Wiley, West Sussex, England.
Gocke, M., U. Hambach, E. Eckmeier, L. Schwark, L. Zöller, M. Fuchs, M. Löscher, and G. L. B. Wiesenberg (2014), Introducing an improved multi-proxy approach for paleoenvironmental reconstruction of loess-paleosol archives applied on the late Pleistocene Nussloch sequence (SW Germany), *Palaeogeogr. Palaeoclimatol. Palaeoecol.*, *410*, 300–315.
Guiter, F., V. Andrieu-Ponel, J. L. de Beaulieu, R. Cheddadi, M. Calvez, P. Ponel, M. Reille, T. Keller, and C. Goeury (2003), The last climatic cycles in western Europe: A comparison between long continuous lacustrine sequences from France and other terrestrial records, *Quat. Int.*, *111*(1), 59–74.
Hatté, C., and J. Guiot (2005), Palaeoprecipitation reconstruction by inverse modelling using the isotopic signal of loess organic matter: Application to the Nußloch loess sequence (Rhine Valley, Germany), *Clim. Dyn.*, *25*, 315–327.
Hext, G. R. (1963), The estimation of second-order tensors, with related tests and designs, *Biometrika*, *50*, 353.
Huijzer, A. S. (1993), Microfabrics and macrostructures: Interrelations, processes, and paleoenvironmental significance. *Thesis*, Vrije Universiteit Amsterdam.
Huijzer, B., and J. Vandenberghe (1998), Climatic reconstruction of the Weichselian Pleniglacial in northwestern and central Europe, *J. Quat. Sci.*, *13*(5), 391–417.
Hunt, C. P., S. K. Banerjee, P. A. Solheid, and W.-W. Sun (1994), Rock-magnetic study of the climate proxy record at Xining in the Chinese loess plateau, north-central China (abstract), *Eos, Trans. AGU*, *75*(44suppl.), 187.
Hus, J. J. (2003), The magnetic fabric of some loess/palaeosol deposits, *Phys. Chem. Earth*, *28*(16), 689–699.
Jelinek, V. (1981), Characterization of the magnetic fabric of rocks, *Tectonophysics*, *79*(3), T63–T67.
Jordanova, N., D. Jordanova, and V. Karloukovski (1996), Magnetic fabric of Bulgarian loess sediments derived by using various sampling techniques, *Stud. Geophys. Geod.*, *40*(1), 36–49.
Juvigné, E., and A. Semmel (1981), Un tuf volcanique semblable à l'Eltviller Tuff dans les loess de Hesbaye et du Limbourg ne´erlandais, *Eiszeitalter Ggw.*, *31*, 83–90.
Kadereit, A., C. J. Kind, and G. A. Wagner (2013), The chronological position of the Lohne Soil in the Nussloch loess section: Re-evaluation for a European loess-marker horizon, *Quat. Sci. Rev.*, *59*, 67–86.
Kligfield, R., W. H. Owens, and W. Lowrie (1981), Magnetic susceptibility anisotropy, strain, and progressive deformation in Permian sediments from the Maritime Alps (France), *Earth Planet. Sci. Lett.*, *55*(1), 181–189.
Lagroix, F., and G. J. Borradaile (2000), Magnetic fabric interpretation complicated by inclusions in mafic silicates, *Tectonophysics*, *325*(3), 207–225.
Lagroix, F., and S. K. Banerjee (2002), Paleowind directions from the magnetic fabric of loess profiles in central Alaska, *Earth Planet. Sci. Lett.*, *195*(1), 99–112.
Lagroix, F., and S. K. Banerjee (2004a), Cryptic post-depositional reworking in aeolian sediments revealed by the anisotropy of magnetic susceptibility, *Earth Planet. Sci. Lett.*, *224*(3–4), 453–459.
Lagroix, F., and S. K. Banerjee (2004b), The regional and temporal significance of primary aeolian magnetic fabrics preserved in Alaskan loess, *Earth Planet. Sci. Lett.*, *225*(3–4), 379–395.

Lang, A., C. Hatté, D. D. Rousseau, P. Antoine, M. Fontugne, L. Zöller, and U. Hambach (2003), High-resolution chronologies for loess: Comparing AMS ^{14}C and optical dating results, *Quat. Sci. Rev.*, *22*, 953–959.
Leger, M. (1990), Loess landforms, *Quat. Int.*, *7*, 53–61.
Liu, X., T. Xu, and T. Liu (1988), The Chinese loess in Xifeng, II. A study of anisotropy of magnetic susceptibility of loess from Xifeng, *Geophys. J. Int.*, *92*(2), 349–353.
Maher, B. A., and R. Thompson (1991), Mineral magnetic record of the Chinese loess and paleosols, *Geology*, *19*(1), 3–6.
Maher, B. A., and R. Thompson (1995), Paleorainfall reconstructions from pedogenic magnetic susceptibility variations in the Chinese loess and paleosols, *Quat. Res.*, *44*(3), 383–391.
Matasova, G., E. Petrovsky, N. Jordanova, V. Zykina, and A. Kapicka (2001), Magnetic study of late Pleistocene loess/palaeosol sections from Siberia: Palaeoenvironmental implications, *Geophys. J. Int.*, *147*(2), 367–380.
Mathé, P. E., P. Rochette, and F. Colin (1997), The origin of magnetic susceptibility and its anisotropy in some weathered profiles, *Phys. Chem. Earth*, *22*(1), 183–187.
Mathé, P. E., P. Rochette, D. Vandamme, and F. Colin (1999), Volumetric changes in weathered profiles: Iso-element mass balance method questioned by magnetic fabric, *Earth Planet. Sci. Lett.*, *167*(3), 255–267.
Moine, O. (2014), Weichselian Upper Pleniglacial environmental variability in north-western Europe reconstructed from terrestrial mollusc faunas and its relationship with the presence/absence of human settlements, *Quat. Int.*, *337*, 90–113.
Moine, O., D. D. Rousseau, and P. Antoine (2005), Terrestrial molluscan records of Weichselian Lower to Middle Pleniglacial climatic changes from the Nussloch loess series (Rhine Valley, Germany): The impact of local factors, *Boreas*, *34*(3), 363–380.
Moine, O., D. D. Rousseau, and P. Antoine (2008), The impact of Dansgaard–Oeschger cycles on the loessic environment and malacofauna of Nussloch (Germany) during the Upper Weichselian, *Quat. Res.*, *70*, 91–104.
Muhs, D. R., S. R. Cattle, O. Crouvi, D. D. Rousseau, J. Sun, and M. A. Zárate (2014), Loess Records, in *Mineral Dust*, pp. 411–441, Springer, Netherlands.
Nagata, T. (1961), *Rock Magnetism*, 2nd ed., 350 pp., Maruzen Company Ltd., Tokyo.
Nawrocki, J., O. Polechonska, A. Boguckij, and M. Łanczont (2006), Palaeowind directions recorded in the youngest loess in Poland and western Ukraine as derived from anisotropy of magnetic susceptibility measurements, *Boreas*, *35*, 266–271.
Paillard, D., L. Labeyrie, and P. Yiou (1996), Macintosh program performs time-series analysis, *Eos Trans. AGU*, *77*, 379.
Pouclet, A., and E. Juvigné (2009), The Eltville Tephra, a late Pleistocene widespread tephra layer in Germany, Belgium and Netherlands: Symptomatic compositions of the minerals, *Geol. Belg.*, *12*, 93–103.
Rochette, P., M. Jackson, and C. Aubourg (1992), Rock magnetism and the interpretation of anisotropy of magnetic susceptibility, *Rev. Geophys.*, *30*(3), 209–226.
Rousseau, D. D., et al. (2002), Abrupt millenial climatic changes from Nussloch (Germany) Upper Weichselian eolian records during the last glaciation, *Quat. Sci. Rev.*, *21*, 1577–1582.
Rousseau, D. D., A. Sima, P. Antoine, C. Hatté, A. Lang, and L. Zöller (2007), Link between European and North-Atlantic abrupt climate changes over the last glaciation, *Geophys. Res. Lett.*, *34*, L22713, doi:10.1029/2007GL031716.
Rousseau, D. D., et al. (2014), European glacial dust deposits: Geochemical constraints on atmospheric dust cycle modeling, *Geophys. Res. Lett.*, *41*, 7666–7674, doi:10.1002/2014GL061382.
Sima, A., D. D. Rousseau, M. Kageyama, G. Ramstein, M. Schulz, Y. Balkanski, P. Antoine, F. Dulac, and C. Hatté (2009), Imprint of North-Atlantic abrupt climate changes on western European loess deposits as viewed in a dust emission model, *Quat. Sci. Rev.*, *28*(25), 2851–2866.
Tarling, D., and F. Hrouda (Eds.) (1993), *Magnetic Anisotropy of Rocks*, Chapman & Hall, London.
Tauxe, L. (2002), *Paleomagnetic Principles and Practice*, 300 pp., Springer, New York.
Taylor, S. N., and F. Lagroix (2014), Mineral magnetic analysis of the Upper Pleniglacial loess-palaeosol deposits from Nussloch (Germany): An insight into local environmental processes, *Geophys. J. Int.*, *199*, 1463–1480.
Tissoux, H., H. Valladas, P. Voinchet, J. L. Reyss, N. Mercier, C. Falgueres, J. J. Bahain, L. Zoller, and P. Antoine (2010), OSL and ESR studies of Aeolian quartz from the Upper Pleistocene loess sequence of Nussloch (Germany), *Quat. Geochronol.*, *5*(2–3), 131–136.
Vandenberghe, J., and A. Pissart (1993), Permafrost changes in Europe during the Last Glacial, *Permafrost Periglac.*, *4*(2), 121–135.
Vandenberghe, J., and G. Nugteren (2001), Rapid climatic changes recorded in loess successions, *Global Planet. Change*, *28*(1), 1–9.
Vandenberghe, J., B. S. Huijzer, H. Mücher, and W. Laan (1998), Short climatic oscillations in a western European loess sequence (Kesselt, Belgium), *J. Quat. Sci.*, *13*(5), 471–485.
Vliet-Lanoë, B. (1991), Chronostratigraphy and paleoclimatic meaning of cryogenic deformations in the central European loess, *GeoJournal*, *24*(2), 157–163.
Vliet-Lanoë, B. V. (1989), Dynamics and extent of the Weichselian permafrost in western Europe (substage 5e to stage 1), *Quat. Int.*, *3*, 109–113.
Zhang, R., V. A. Kravchinsky, R. Zhu, and L. Yue (2010), Paleomonsoon route reconstruction along a W-E transect in the Chinese Loess Plateau using the anisotropy of magnetic susceptibility: Summer monsoon model, *Earth Planet. Sci. Lett.*, *299*(3), 436–446.
Zhou, L. P., F. Oldfield, A. G. Wintle, S. G. Robinson, and J. T. Wang (1990), Partly pedogenic origin of magnetic variations in Chinese loess, *Nature*, *346*, 737–739.
Zhu, R., Q. Liu, and M. J. Jackson (2004), Paleoenvironmental significance of the magnetic fabrics in Chinese loess-paleosols since the last interglacial (<130 ka), *Earth Planet. Sci. Lett.*, *221*(1), 55–69.